To be published in Optics Letters:

Title: Protein sensing using deep subwavelength-engineered photonic crystals

Authors: Yanrong Zhang,Christopher Whittington,Rabeb Layouni,Andres Cotto,Kellen Arnold,Sami Halimi,Sharon Weiss

Accepted: 04 December 23

Posted 05 December 23

DOI: https://doi.org/10.1364/OL.510541

Protein sensing using deep subwavelength-engineered photonic crystals

YANRONG ZHANG[1], CHRISTOPHER S. WHITTINGTON[2], RABEB LAYOUNI[3], ANDRES M. COTTO[4], KELLEN P. ARNOLD[2], SAMI I. HALIMI[1], AND SHARON M. WEISS[*1,2]

[1]*Department of Electrical and Computer Engineering, Vanderbilt University, Nashville, Tennessee 37235, USA*
[2] *Interdisciplinary Materials Science Program, Vanderbilt University, Nashville, Tennessee 37235, USA*
[3]*Department of Chemical and Biomolecular Engineering, Vanderbilt University, Nashville, Tennessee 37235, USA*
[4]*Department of Chemical, Biological, and Materials Engineering, University of South Florida, Tampa, FL*

**Corresponding author: sharon.weiss@vanderbilt.edu*

We demonstrate higher sensitivity detection of proteins in a photonic crystal platform by including a deep subwavelength feature in the unit cell that locally increases the energy density of light. Through both simulations and experiments, the sensing capability of a deep subwavelength-engineered silicon antislot photonic crystal nanobeam (PhCNB) cavity is compared to that of a traditional PhCNB cavity. The redistribution and local enhancement of the energy density by the 50 nm antislot enables stronger light-molecule interaction at the surface of the antislot and leads to a larger resonance shift upon protein binding. This surface-based energy enhancement is confirmed by experiments demonstrating a nearly 50% larger resonance shift upon attachment of streptavidin molecules to biotin-functionalized antislot PhCNB cavities.

Optical biosensors have been widely reported for their ability to sensitively detect various molecules including DNA, proteins, and viruses [1,2]. While surface plasmon resonance [3] and fluorescence-based [4] biosensors remain among the most common optical biosensor platforms, there is increasing interest in on-chip label-free optical biosensing platforms that are compatible with scalable fabrication and multiplexed detection of biomolecules [5,6]. In particular, ring resonator biosensors have been extensively studied and commercialized for label-free detection of nucleic acid molecules, viruses, cancer biomarkers, and various chemical compounds [7–11]. Significant progress has been reported with slotted ring resonators and subwavelength grating-based ring resonators, which can achieve higher detection sensitivity than traditional ring resonators [12–15]. Photonic crystal-based optical biosensors have also been studied and photonic crystal nanobeam (PhCNB) biosensors in particular offer a more compact alternative for higher density multiplexing with the potential to realize high sensitivity detection of biomolecules using only a small volume of analyte delivered to the low mode volume cavity region [16–18]. Notably, most demonstrations of on-chip optical biosensors utilize silicon or silicon nitride substrates and hence the surface chemistry and functionalization reported on the more mature ring resonator biosensor technology can be directly applied to PhCNB biosensors for the detection of various biological molecules.

Previous studies have shown that deep subwavelength engineering inside the PhCNB cavity unit cells can enhance light-matter interaction by redistributing the electric field energy, which could significantly improve surface detection sensitivity when such structures are applied for biosensing applications [19–21]. However, to date, optical biosensing with deep subwavelength engineered PhCNB cavities has not been demonstrated. This paper focuses on how the incorporation of an antislot (i.e., 50 nm silicon bar) into a circular PhC unit cell improves surface-based molecular detection capabilities. Through direct comparison with a traditional PhCNB cavity, finite-difference time-domain (FDTD) simulations and perturbation theory calculations show an increase in surface-based detection sensitivity for an antislot PhCNB cavity. Furthermore, in experiment, antislot PhCNB cavities demonstrate larger resonance shifts than traditional PhCNB cavities in a biotin-streptavidin assay. As the minimum feature size achievable in scalable deep-ultraviolet lithography processes for photonics components continues to decrease [22], the development of biosensors based on integrated photonics incorporating deep-subwavelength engineereed PhC cavities can contribute to the realization of a widely-accessible and highly sensitive platform for the detection of pathogens and other biological molecules.

Similar to what we reported previously [20], and following the deterministic design approach [23], we designed both traditional and antislot PhCNB cavities for air mode operation with a target fundamental resonance wavelength near 1550 nm using MIT Photonic Bands and Anysis Lumerical FDTD simulations. The PhCNB cavities were designed for transverse electric (TE) polarized light. The two types of PhCNB cavities, fabricated using standard electron beam lithography and reactive ion etching processes on

silicon-on-insulator (SOI) wafers with a 220 nm silicon device layer, are shown in Fig. 1a-b. The designed traditional silicon PhCNB cavity consists of a periodic array of air holes in a silicon nanobeam. The nanobeam width was deterministically tapered from 830 nm at the central cavity unit cell to 690 nm at the end mirror unit cells to form a cavity with an instrinsic quality factor near 1.5×10^4. Fourteen tapering unit cells were included on each side of the cavity with no additional end mirror unit cells. The radius of the air holes was fixed at 96 nm and the lattice spacing was 360 nm. The designed antislot PhCNB cavity incorporating circular unit cells with 50 nm wide antislots was formed by deterministically rotating the antislot unit cells from from 90 to 0 degrees (i.e., from orthogonal to parallel to the propagation direction) between the central unit cell and the end mirror unit cells. The ability to change the band structure of the PhCNB via unit cell rotation is a unique capability of these subwavelength-engineered PhCNBs [19]. With eighteen tapering unit cells on each side of the cavity and three additional end mirror unit cells, the instrinsic quality factor was near 1.5×10^4. In this configuration, the air holes had a fixed radius of 112 nm and the lattice spacing was 360 nm.

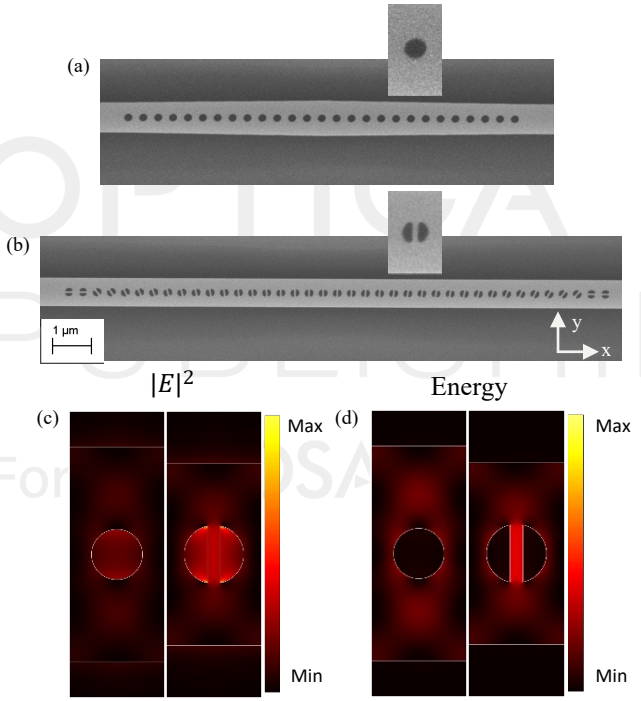

Fig. 1. SEM images of (a) traditional PhCNB cavity and (b) antislot PhCNB cavity. The insets are the zoom-in images of the central unit cell of each PhCNB cavity. (c) Electric field and (d) energy distribution for traditional and antislot PhCNB cavities.

Figure 1c-d shows the electric field and energy distributions in the traditional and antislot PhCNB central cavity unit cells, which were calculated with three-dimensional (3D) FDTD simulations. For each type of unit cell, a TE dipole source, offset from the unit cell center and located in air, was utilized for excitation and a field monitor was used to record the electric field distribution and Purcell enhancement. Periodic boundary conditions in the x-direction and perfectly matched layers in both the y- and z-directions were employed. Based on the minimum feature sizes in each design, a 2 nm mesh step was used for the tradiational PhCNB while a 1 nm mesh step was used for the antislot PhCBN. To enable a fair comparison of the electric field distributions in the two different unit cells, we plotted the square of the electric field divided by the respective Purcell factor of the unit cell (Fig. 1c), which normalized the dipole power to be equal in both unit cells. The same procedure was carried out to normalize the energy density plots (Fig. 1d). Consistent with prior work [19], the electric field distribution is relatively uniform across both types of unit cells but the energy density is significantly enhanced in the antislot by a factor of approximately 25 compared to the energy density in the center of the traditional PhCNB unit cell. For sensing applications, it is most relevant to compare the energy density at specific locations in each of the PhCNB unit cells that are accessible for molecule attachment. Here we compare the energy density in the air region at the sidewall of the antislot in the antislot PhCNB to the energy density in the air region at the inner surface of the circular air hole of the traditional PhCNB; the simulations suggest an approximately 40% enhancement for the antislot PhCNB cavity unit cell.

To better understand how the energy density enhancement affects the performance of antislot PhCNB cavities compared to traditional PhCNB cavities, we investigated through simulations and experiments both bulk sensing and surface sensing cases. For bulk sensing, we immerse PhCNB cavities in water, which changed the dielectric environment from air to water. For surface sensing, we carried out a biotin-streptavidin assay. Because deep subwavelength engineering inside the PhC unit cell redistributes energy according to electromagnetic boundary conditions and therefore does not significantly alter the total energy [24], it is expected that changing the refractive index of the entire dielectric environment will lead to a similar resonance wavelength shift for traditional and antislot PhCNB cavities. However, for surface sensing, the energy density at the surface plays a key role in determining the magnitude of the resonance shift; accordingly, with a higher energy density at the surface of the antislot compared to the surface of the traditional PhC unit cell, it is anticipated that the antislot PhCNB cavity will have a larger resonance shift than the traditional PhCNB cavity for surface sensing applications.

First, we consider the bulk sensing case. In 3D FDTD simulations, a fundamentional TE mode source was added on the input side of the PhCNBs and a frequency domain power monitor was added on the output side in the y-z plane. For most of the simulation area, an automatically generated non-uniform mesh was carried out, with a mesh size ranging from 50 to 100 nm. The region containing the array of holes within both the traditional and antislot PhCNB cavities was assigned a uniform mesh size of 10 nm. As shown in Fig. 2a, the simulated transmission spectra for both types of PhCNBs red-shifted to longer wavelengths when the dielectric environment was changed from air (n=1) to water (n=1.313). The fundamental resonance of the traditional PhCNB cavity shifted by 35.5 nm while the fundamental resonance of the antislot PhCNB cavity shifted by 39.1 nm; moreover, higher order resonances red-shifted into the simulated spectral bandwidth in water. This result matches expectations that an overall change in the dielectric environment leads to similar light-matter interaction and fundamental resonance shift for both types of PhCNB cavities. Good agreement between simulation and experiments was found, as shown in Fig. 2b. Transmission measurements were carried out with TE-light from a tunable laser (Santec TSL-510), edge-coupled polarization-maintaining lensed input/output fibers (OZ Optics), and an optical

power meter (Newport 2936-R). The fundamental resonance of the fabricated traditional PhCNB cavity had a loaded Q = 3000 and red-shifted by 31.4 nm when immersed in water while the fundamental resonance of the fabricated antislot PhCNB cavity had a loaded Q = 3000 and red-shifted by 32.8 nm when immersed in water. The slightly different resonance wavelengths and lower Q resonances for the fabricated PhCNB cavities compared to the simulated PhCNB cavities were attributed to slight differences in the designed and fabricated dimensions and additional losses introduced during the fabrication process. The lower Q fabricated cavities also exhibited smaller shifts than those in simulation due to reduced temporal light-matter interaction.

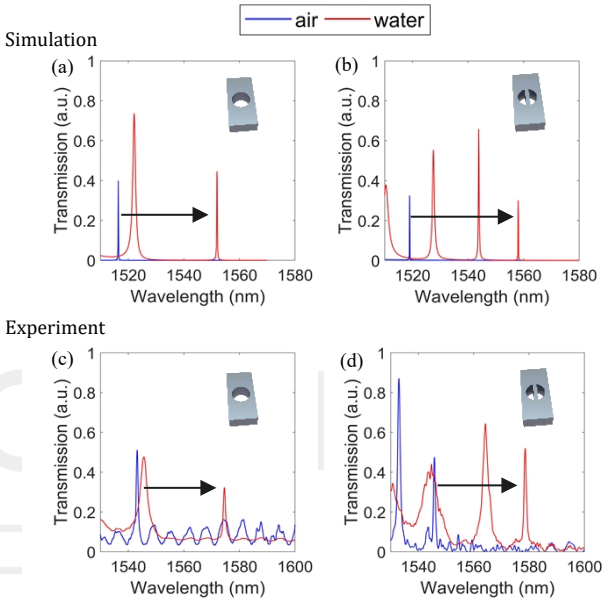

Fig. 2. Simulated transmission spectra of (a) traditional and (b) antislot silicon PhCNB cavities in air (blue) and water (red). Experimental transmission spectra of (c) traditional and (d) antislot PhCNB cavities in air (blue) and water (red). Arrows indicate the shift of the fundamental resonance.

Next, we consider the surface sensing case. We utilized a computationally efficient 3D perturbation approach based on Eqn. 1 to determine the expected resonance shifts of the traditional and antislot PhCNB cavities when molecules attach to the surface (details provided in Supplement 1).

$$\Delta\omega = -\frac{\omega \int_V \Delta\varepsilon(r)|E(r)|^2 \, d^3r}{2 \int_V \varepsilon(r)|E(r)|^2 \, d^3r} \quad (1)$$

The 3D FDTD simulation results for the traditional and antislot PhCNB cavities in air presented in Fig. 2 were combined with a similar 3D FDTD simulation carried out with a 3D volumetric index monitor for each type of PhCNB cavity to find the initial, unperturbed electric field distribution ($|E|^2$) and the permittivity at every mesh point (ε) at the initial fundamental resonant frequency (ω). Different thickness layers with $n = 1.46$ were then added to the PhCNB surfaces in the perturbation model to mimic the attachment of biomolecules with an assumed 100% packing density, and the respective change in permittivity at each spatial mesh point was used to determine $\Delta\varepsilon$ [20]. As shown in Fig. 3, the perturbation theory results demonstrate that the antislot PhCNB cavity has a higher detection sensitivity for molecular surface capture compared to the traditional PhCNB cavity. This result matches expectations as the increased sensitivity is attributed to the enhanced light-matter interaction at the surfaces of the antislot PhCNB (Fig. 1). 3D FDTD simulations were carried out for traditional and antislot PhCNB cavities with added surface layers of three different thicknesses to validate the 3D perturbation theory results; good agreeement is shown between perturbation and FDTD results (Fig. 3). We note that the slight nonlinearity in the relationship between the resonance shift and the surface layer thickness is due in part to the nonlinear decrease in electric field intensity as a function of distance from the surfaces of the PhCNBs.

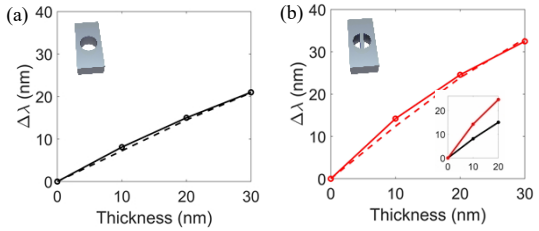

Fig. 3. Simulated resonance shifts of (a) traditional and (b) antislot PhCNB cavity with different thickness monolayers (n = 1.46) attached on all surfaces of the PhCNBs. The dashed lines show the computationally efficient 3D perturbation calculation and the solid lines show guides to the eye for the discrete 3D FDTD simulation results. The inset shows a zoomed-in region comparing the simulated resonance shifts of the traditional (black) and antislot (red) PhCNB cavity for 0 – 20 nm surface layer attachment.

To confirm the calculated results for surface sensing, traditional and antislot PhCNB cavities were functionalized for the selective capture of streptavidin protein molecules. The surfaces of the PhCNB cavities were first oxidized with a 10 minute soak in piranha solution. Next, the oxidized samples were soaked in 4% 3-aminopropyltriethoxysilane solution for 15 minutes, followed by a 15 minute soak in methanol to remove unbound molecules, and annealing for 15 minutes at 150 °C in air to promote cross-linking. Sulfo-N-hydroxysulfosuccinimide-biotin (0.01 mg/mL) was then introduced to the amine terminated samples and reacted for 1 hour to anchor the biotin capture probes. Finally, the biotin-modified PhCNB cavities were exposed to a 20 μM streptavidin solution in deionized water for 2 hours and subsequently soaked in deionized water for 2 hours to remove unbound protein molecules.

As shown in Fig. 4, the antislot PhCNB cavity gives a larger resonance shift upon streptavidin binding on the sensor surface compared to the traditional PhCNB cavity. Considering the average resonance shift of 4 samples, the antislot PhCNB cavity sensors demonstrate a 45% larger resonance shift, which is consistent with expectations from the energy density enhancement near the active sensing surfaces shown in Fig. 1. Referring to Eqn. 1, an increase in energy desnity directly correlates to an increase in the magnitude of the resonance shift resulting from molecular attachment. The fundamental resonance wavelength of antislot PhCNB cavity sensors shifts by ≈ 2.5 nm due to streptavidin attachment while that of the traditional PhCNB cavity sensors shifts by ≈ 1.7 nm. If we assume streptavidin molecules are approximately 5 nm in size, then we find reasonable agreement with the shifts predicted by simulations in Fig. 3, noting that streptavidin attachment is not expected to provide a complete monolayer coverage [25]. By

comparing the experimentally measured resonance shifts to the simulated resonance shifts for a 5 nm monolayer of biomolecules, we estimate coverage percentages of streptavidin molecules on the antislot and traditional PhCNB cavities to be approximately 40% and 60%, respectively. The lower surface coverage of streptavidin on the antislot PhCNB cavities is attributed to the more constricted geometry inside the antislot PhCNB unit cell compared to the traditional PhCNB unit cell, which hinders molecular diffusion and attachment to the inner surfaces [20].

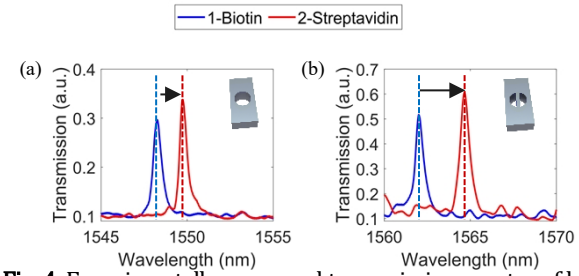

Fig. 4. Experimentally measured transmission spectra of biotin-functionalized (a) traditional and (b) antislot silicon PhCNB cavity sensors before and after exposure to streptavidin protein.

In conclusion, we report improved molecular surface sensing capabilities of antislot PhCNB cavity sensors compared to traditional PhCNB cavity sensors. The enhanced energy density in the deep subwavelength-scale antislot leads to stronger field-molecule interactions in the evanescent field near the antislot. The antislot effect that causes the field redistribution throughout the unit cell and enhancement in the antislot, as shown in perturbation theory calculations and FDTD simulations, is experimentally validated by the demonstration of the similar bulk sensing sensitivity but enhanced surface sensing sensitivity of the antislot PhCNB compared to the traditional PhCNB cavity sensor.

Funding. National Science Foundation (ECCS1809937, DMR1852157).

Acknowledgments. Photonic crystals were fabricated at the Center for Nanophase Materials Sciences, which is a US Department of Energy, Office of Science User Facility at Oak Ridge National Laboratory. SEM images were taken in the Vanderbilt Institute of Nanoscale Science and Engineering (VINSE). The authors thank Hang Shi for guidance on the python script used in the PhCNB design and Dr. Scott Retterer for assistance with PhCNB fabrication. A. M. Cotto's contributions to this work were supported by the VINSE NSF REU program.

Disclosures. The authors declare no conflicts of interest.

Data availability. Data underlying the results presented in this paper are not publicly available at this time but may be obtained from the authors upon reasonable request.

Supplemental document. See Supplement 1 for supporting content.

References

1. S. M. Borisov and O. S. Wolfbeis, Chem. Rev. **108**, 423 (2008).
2. C. Chen and J. Wang, Analyst. **145**, 1605 (2020).
3. H. H. Nguyen, J. Park, S. Kang, and M. Kim, Sensors (Switzerland) **15**, 10481 (2015).
4. B. H. Jun, H. Kang, Y. S. Lee, and D. H. Jeong, Molecules **17**, 2474 (2012).
5. K. Zinoviev, L. Carrascosa, J. del Río, B. Sepulveda, C. Domínguez, and L. Lechuga, Adv. Opt. Technol. **2008**, 383927, (2008).
6. E. Luan, H. Shoman, D. M. Ratner, K. C. Cheung, and L. Chrostowski, Sensors **18**, 3519 (2018).
7. A. L. Washburn, L. C. Gunn, and R. C. Bailey, Anal. Chem. **81**, 9499 (2009).
8. S. Mudumba, S. de Alba, R. Romero, C. Cherwien, A. Wu, J. Wang, M. A. Gleeson, M. Iqbal, and R. W. Burlingame, J. Immunol. Methods **448**, 34 (2017).
9. A. J. Qavi, J. T. Kindt, M. A. Gleeson, and R. C. Bailey, Anal. Chem. **83**, 5949 (2011).
10. M. S. McClellan, L. L. Domier, and R. C. Bailey, Biosens. Bioelectron. **31**, 388 (2012).
11. P. Steglich, M. Hülsemann, B. Dietzel, and A. Mai, Molecules **24**, 519 (2019).
12. J. G. Wangüemert-Pérez, P. Cheben, A. Ortega-Moñux, C. Alonso-Ramos, D. Pérez-Galacho, R. Halir, I. Molina-Fernández, D.-X. Xu, and J. H. Schmid, Opt. Lett. **39**, 4442 (2014).
13. J. Flueckiger, S. Schmidt, V. Donzella, A. Sherwali, D. M. Ratner, L. Chrostowski, and K. C. Cheung, Opt. Express **24**, 15672 (2016).
14. H. Yan, L. Huang, X. Xu, S. Chakravarty, N. Tang, H. Tian, and R. T. Chen, Opt. Express **24**, 29724 (2016).
15. C. A. Barrios, Sensors **9**, 4751 (2009).
16. W.-C. Lai, S. Chakravarty, Y. Zou, and R. T. Chen, Opt. Lett **37**, 1208 (2012).
17. Q. Qiao, J. Xia, C. Lee, and G. Zhou, Micromachines (Basel) **9**, 541 (2018).
18. H. Inan, M. Poyraz, F. Inci, M. A. Lifson, M. Baday, B. T. Cunningham, and U. Demirci, Chem. Soc. Rev. **46**, 366 (2017).
19. S. Hu and S. M. Weiss, ACS Photonics **3**, 1647 (2016).
20. Y. Zhang, R. Layouni, C. S. Whittington, S. I. Halimi, and S. M. Weiss, in Proc. SPIE **12397**, 1239703 (2023).
21. S. Hu, M. Khater, R. Salas-Montiel, E. Kratschmer, S. Engelmann, W. M. J. Green, and S. M. Weiss, Sci. Adv. **4**, eaat2355 (2018).
22. J. A. Allen, K. P. Arnold, S. I. Halimi, L. D. Ryder, F. O. Afzal, Y. Bian, A. Aboketaf, K. Dezfulian, M. Rakowski, R. Augur, T. Hirokawa, K. Nummy, and S. M. Weiss, IEEE Photonics Technol. Lett. **35**, 461 (2023).
23. Q. Quan and M. Loncar, Opt. Express **19**, 18529 (2011).
24. S. Hu, M. Khater, E. Kratschmer, S. Engelmann, W. M. J. Green, and S. M. Weiss, Opt. Express **30**, 7612 (2022).
25. P. H. E. Hamming and J. Huskens, ACS Appl. Mater. Interfaces. **13**, 58114 (2021).